Acta Cryst B
STRUCTURAL SCIENCE
CRYSTAL ENGINEERING
MATERIALS
ISSN 2052-5206

Crystal structure, absolute configuration and characteristic temperatures of $SmFe_3(BO_3)_4$ in the temperature range 11–400 K

Ekaterina S. Smirnova,[a]* Olga A. Alekseeva,[a] Alexander P. Dudka,[a] Timofei A. Sorokin,[a] Dmitry N. Khmelenin,[a] Vasily O. Yapaskurt,[b] Marianna V. Lyubutina,[a] Kirill V. Frolov,[a] Igor S. Lyubutin[a] and Irina A. Gudim[c]

[a]Shubnikov Institute of Crystallography of Federal Scientific Research Centre 'Crystallography and Photonics', Russian Academy of Sciences, Moscow 119333, Russian Federation, [b]Moscow State University, Faculty of Geology, Moscow 119991, Russian Federation, and [c]Kirensky Institute of Physics, Federal Research Center KSC SB RAS, Krasnoyarsk 660036, Russian Federation. *Correspondence e-mail: esmi@ns.crys.ras.ru

Received 12 February 2022
Accepted 11 April 2022

Edited by A. Katrusiak, Adam Mickiewicz University, Poland

Keywords: samarium bismuth iron borate; absolute configuration; crystal structure; multi-temperature single-crystal X-ray diffraction; Mössbauer spectroscopy; characteristic temperatures; solution-melt growth.

CCDC references: 2165912; 2165913; 2165914; 2165915; 2165916

Supporting information: this article has supporting information at journals.iucr.org/b

The crystal structure of samarium iron borate was analyzed with regard to growth conditions and temperature. The inclusion of about 7% Bi atoms in the crystals grown using the $Bi_2Mo_3O_{12}$-based flux was discovered and there were no impurities in the crystals grown using the Li_2WO_4-based flux. No pronounced structural features associated with Bi inclusion were observed. The different absolute configurations of the samples grown using both fluxes were demonstrated. Below 80 K, a negative thermal expansion of the *c* unit-cell parameter was found. The structure of $(Sm_{0.93}Bi_{0.07})Fe_3(BO_3)_4$ belongs to the trigonal space group *R*32 in the temperature range 90–400 K. A decrease in the (Sm,Bi)—O, Sm—B, Sm—Fe, Fe—O, Fe—B and Fe—Fe distances is observed with a lowering of the temperature, B1—O does not change, B2—O increases slightly and the $B2O_3$ triangles deviate from the *ab* plane. The strongest decrease in the equivalent isotropic atomic displacement parameters (U_{eq}) with decreasing temperature is observed for atoms Sm and O2, and the weakest is observed for B1. The O2 atoms have the highest U_{eq} values, the most elongated atomic displacement ellipsoids of all the atoms and the smallest number of allowed vibrational modes of all the O atoms. The largest number of allowed vibrational modes and the strongest interactions with neighbouring atoms is seen for the B atoms, and the opposite is seen for the Sm atoms. The quadrupole splitting $\Delta(T)$ of the paramagnetic Mössbauer spectra increases linearly with cooling. The Néel temperature [T_N = 31.93 (5) K] was determined from the temperature dependence of the hyperfine magnetic field $B_{hf}(T)$, which has a non-Brillouin character. The easy-plane long-range magnetic ordering below T_N was confirmed.

1. Introduction

Rare-earth iron borates $RFe_3(BO_3)_4$ (*R* is rare earth) having two magnetic subsystems (*R* and Fe) are referred to as the multiferroic family due to demonstrating different types of magnetic ordering and spin reorientation, mutual correlations of transport and magnetic ordering phenomena. These features are explained by the interaction between rare-earth ions and iron ions, which has a pronounced anisotropic character (Kadomtseva *et al.*, 2010). $SmFe_3(BO_3)_4$ was classified as a multiferroic based on the presence of spontaneous polarization and mutually correlated magnetoelectric and magnetoelastic properties (Popov *et al.*, 2010). Among rare-earth iron borates, it is distinguished by a large value of polarization (about 500 μC m^{-2}) induced by a magnetic field,

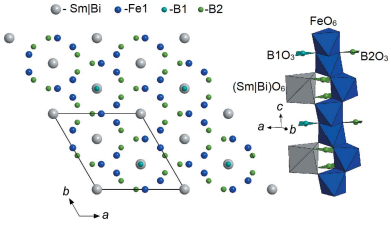

which is related to an easy-plane anisotropy (Popov *et al.*, 2010).

Mukhin *et al.* (2011) observed in $SmFe_3(BO_3)_4$ a very large magnetodielectric effect, which is evidenced by the sharp (about three times) increase in the dielectric constant ε at $T < T_N$ and its suppression to the primary level of the paramagnetic state in a magnetic field of ~5 kOe applied in the basal *ab* plane. In addition, it was shown that the large magnetodielectric effect is induced by the contribution to the dielectric constant ε from the electric susceptibility related to the rotation of magnetic moments in the *ab* plane upon the antiferromagnetic ordering of the Fe^{3+} ions, which is suppressed by a magnetic field. The high value of this effect in samarium iron borate was explained by the relatively high electric polarization in the basal plane, to which the rare-earth system (Sm) contributes predominantly (Mukhin *et al.*, 2011).

The crystal structure of rare-earth iron borates $RFe_3(BO_3)_4$ at high temperatures belongs to the trigonal space group *R*32. This space group persists for the iron borates with a large ionic radius of the rare-earth element (*R* = La, Ce, Pr, Nd and Sm) down to 3–4 K, whereas for the iron borates with a smaller ionic radius (*R* = Eu, Gd, Tb, Dy, Ho, Er and Y) there is a structural phase transition to the trigonal space group $P3_121$ (or the $P3_221$ enantiomorphic modification). The temperature of the structural phase transition decreases linearly with increasing ionic radius of the rare-earth element (Kadomtseva *et al.*, 2010).

The structure of rare-earth iron borates in the space group *R*32 comprises layers of *R* (Wyckoff position 3*a*) and Fe (Wyckoff position 9*d*) atoms alternating with layers of BO_3 groups (Campá *et al.*, 1997; Klimin *et al.*, 2005; Smirnova *et al.*, 2022). There are two types of B atoms in the structure: B1 (Wyckoff position 3*b*) in the equilateral BO_3 triangle parallel to the *ab* plane and B2 (Wyckoff position 9*e*) in the isosceles BO_3 triangle slightly deviated from the *ab* plane, with three different Wyckoff positions for the O atoms. The *R* atoms are in slightly distorted RO_6 trigonal prisms, whose bases are parallel to the *ab* plane and are rotated relative to each other. All the *R*—O distances in the prism are the same. The Fe atoms are in distorted FeO_6 octahedra. These octahedra are connected by their edges and form chiral chains in the *c*-axis direction. After the structural transition to the $P3_121$ space group, the threefold axis passing through the *R* and B1 atoms disappears. The B2 atom position splits into two types [B2 (Wyckoff position 6*c*) and B3 (Wyckoff position 3*b*)] and the Fe1 atom splits into Fe1 (Wyckoff position 3*a*) and Fe2 (Wyckoff position 6*c*). Seven independent positions appear for the O atoms (Klimin *et al.*, 2005; Smirnova *et al.*, 2019).

It was demonstrated for neodymium iron borate that the distances in the RO_6 prisms, FeO_6 octahedra and Fe–Fe chains decrease slightly with a lowering of the temperature in the *R*32 space group, the B1—O distances do not change noticeably and the average B2—O distance increases slightly (Smirnova *et al.*, 2022). After the structural phase transition to the space group $P3_121$ (for example, in holmium iron borate), and with a further decrease in temperature, the distortion of the RO_6 prisms, the $Fe1O_6$ and $Fe2O_6$ octahedra, and the $B2O_3$ and $B3O_3$ triangles increases. The $B1O_3$ triangles remain almost equilateral. All the BO_3 triangles deviate from the *ab* plane, with the $B2O_3$ and $B3O_3$ triangles exhibiting the greatest deviations. The changes in the distances and angles in the Fe1 and Fe2 chains are not the same. The Fe1—Fe1 distances in the Fe1 chains decrease with decreasing temperature, while the Fe2—Fe2 distances in the Fe2 chains increase (Smirnova *et al.*, 2019).

Thus, $SmFe_3(BO_3)_4$ is a boundary compound that retains the *R*32 space group, which was confirmed by spectroscopic studies in the temperature range 1.7–300 K (Chukalina *et al.*, 2010) and high-resolution powder neutron diffraction in the temperature range 2–300 K (Ritter *et al.*, 2012). In addition, Hinatsu *et al.* (2003) revealed in $SmFe_3(BO_3)_4$ an antiferromagnetic phase transition at $T = 32$ K (by measuring the magnetic susceptibility) or at $T = 33$ K (by measuring the specific heat). Later, Ritter *et al.* (2012) demonstrated that $SmFe_3(BO_3)_4$ becomes magnetically ordered below 34 K, with a purely easy-plane arrangement. Adjacent layers in the *c* direction are ordered antiferromagnetically. There is a strong Sm–Fe exchange coupling and the magnetic ordering of both Sm and Fe occurs simultaneously. The angle between the Sm and Fe magnetic substructures is about 70°.

Previously, it was assumed (Popova *et al.*, 2016; Erofeev *et al.*, 2016) that Bi impurity is incorporated into $RFe_3(BO_3)_4$ single crystals grown by the solution-melt technique from the $Bi_2Mo_3O_{12}$-based flux (Gudim *et al.*, 2010). This was confirmed by energy-dispersive X-ray spectroscopy (EDS) and single-crystal X-ray structure analysis (Smirnova *et al.*, 2016, 2018, 2019, 2022). Bismuth incorporation leads to a decrease in the structural phase transition temperature T_s, since bismuth has a larger ionic radius than the rare-earth elements in the $RFe_3(BO_3)_4$ (*R* = Eu–Er and Y) structures. Therefore, the T_s value in mixed iron borates $R_{1-x}R'_xFe_3(BO_3)_4$ can be tuned by varying the value of *x* in the crystal composition. This effect can be implemented for switches and optical storage devices (Boldyrev *et al.*, 2021).

Similarly, the incorporation of Bi^{3+} and Mo^{3+} atoms into the structure of isostructural rare-earth aluminium borates $RAl_3(BO_3)_4$ grown using a $Bi_2Mo_3O_{12}$-based flux, as well as the incorporation of Mo^{3+} atoms into $RAl_3(BO_3)_4$ grown using a $K_2Mo_3O_{10}$-based flux, was found (Boldyrev *et al.*, 2012).

Recently, a novel Li_2WO_4-based flux was used for growing $RFe_3(BO_3)_4$ single crystals in order to avoid Bi incorporation in the structure (Eremin *et al.*, 2019; Boldyrev *et al.*, 2021).

The difference between the optical spectra of $EuFe_3(BO_3)_4$ grown with the novel Li_2WO_4-based flux and $EuFe_3(BO_3)_4$ grown with the conventional $Bi_2Mo_3O_{12}$-based flux was demonstrated by high-resolution temperature-dependent polarized optical spectroscopy. The studies were carried out in the temperature range of the paramagnetic phase $T > T_s = 84$ K (space group *R*32) and $T_s > T > T_N = 34$ K (space group $P3_121$), as well as for the antiferromagnetic phase ($T < T_N$) (Popova *et al.*, 2016).

A distinctive characteristic of chiral Sohncke-type space groups $P3_121$ ($P3_221$) and *R*32 (*Online Dictionary of Crystallography*, 2017, 2019*a*) is the presence of threefold screw

axes, which defines a number of physical phenomena. Chirality can affect the optical rotatory power (Condon, 1937), as well as the emergence of ferroelectricity in multiferroics (Cheong & Mostovoy, 2007). A multidomain crystal structure can significantly impair the multiferroic properties of a crystal due to the mutual influence of subdomains. In particular, the magnitude of spontaneous electric polarizations in the $SmFe_3(BO_3)_4$ crystals studied by Popov *et al.* (2010) depended significantly on the choice of the sample (Popova *et al.*, 2017).

The magnetic and magnetoelectric properties of $SmFe_3(BO_3)_4$ single crystals grown using the novel Li_2WO_4-based flux were first studied by Eremin *et al.* (2019). It was found that the magnetoelectric response in $SmFe_3(BO_3)_4$:Bi [*i.e.* Bi-containing $SmFe_3(BO_3)_4$ grown from flux based on $Bi_2Mo_3O_{12}$] is greater than in $SmFe_3(BO_3)_4$ (grown from flux based on Li_2WO_4) by about 1.5 times. The main reason for this effect was related to the different ratio of the twin components, which was 0:100 for $SmFe_3(BO_3)_4$:Bi and 82:18 for $SmFe_3(BO_3)_4$. To a lesser extent, local distortions of the anionic environment of the rare-earth ion due to the presence of the Bi^{3+} impurity could have some effect on the magnetoelectric response.

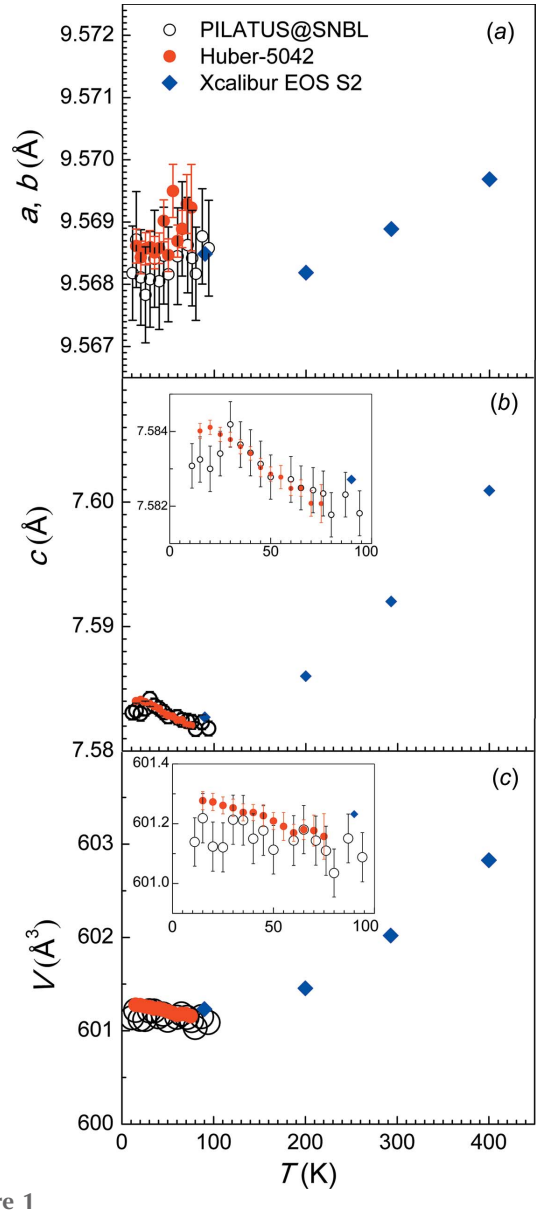

Figure 1
Temperature dependence of the unit-cell parameters (*a*) *a* and *b*, (*b*) *c* and (*c*) volume *V* of the unit cell of samarium iron borate. Single crystals prepared from bismuth-containing **sample 2** were used for measurements on laboratory Xcalibur and Huber diffractometers, and **sample 7(2)** (without Bi) was measured using a PILATUS diffractometer and synchrotron radiation.

There are not so many reports devoted to the characterization of microdomains of rare-earth iron borates. In our previous articles (Smirnova *et al.*, 2016, 2018, 2019, 2022), it was noted that the samples of $RFe_3(BO_3)_4$ (R = Gd, Y, Ho and Nd) selected for single-crystal X-ray structure analysis were merohedral (racemic) twins with almost equal parts of enantiomorphic substructures. Optical activity measurements on the $SmFe_3(BO_3)_4$ single crystal by Platunov *et al.* (2021) revealed possible internal merohedral or nonmerohedral twinning in these crystals.

Having studied $DyFe_3(BO_3)_4$ with the structural phase transition $R32 \rightarrow P3_121$ at T_s = 285 K by resonant X-ray diffraction (RXD), Usui *et al.* (2014) developed a technique to analyze the symmetry-breaking effects that arise due to chirality. This study provided evidence for a helix chiral motif of Dy^{3+} 4*f* quadrupole moments developed in the crystallographic helix chirality. It was also demonstrated that one of the studied samples is practically single domain, while the second contains submillimetre domains of different orientations. Further analysis of the chirality of the Dy^{3+} ions in the $DyFe_3(BO_3)_4$ structure was performed in Popova *et al.* (2017) by high-resolution polarized temperature-dependent optical spectroscopy and theoretical studies. Popova *et al.* (2017) calculated the temperature dependences of the electronic quadrupole moments of the Dy^{3+} ions and showed that the quadrupole helix chirality can be explained quantitatively.

In this article, we analyze the absolute configuration of different samples of $SmFe_3(BO_3)_4$ crystals, and compare the chemical composition and atomic structure of $SmFe_3(BO_3)_4$ grown using $Bi_2Mo_3O_{12}$-based and novel Li_2WO_4-based fluxes. A detailed study of the temperature-dependent structural changes and Mössbauer hyperfine parameters over a wide temperature range was carried out for the sample grown using the $Bi_2Mo_3O_{12}$-based flux.

2. Experimental

2.1. Crystal growth

Single crystals of $SmFe_3(BO_3)_4$ were grown by the solution-melt technique (Gudim *et al.*, 2010; Eremin *et al.*, 2019). The conventional bismuth trimolybdate $Bi_2Mo_3O_{12}$-based flux was used to grow the first series of samples. For the growth of the second series, the novel lithium tungstate Li_2WO_4-based flux was used to avoid incorporation of Bi atoms into the structure.

The flux systems can be expressed in the quasi-binary form:

78% mass [$Bi_2Mo_3O_{12}$ + 3.2B_2O_3 + 0.5Sm_2O_3] + 22% mass $SmFe_3(BO_3)_4$ (1)
75% mass [Li_2WO_4 + 3.6B_2O_3 + 0.3Sm_2O_3] + 25% mass $SmFe_3(BO_3)_4$ (2).

The saturation temperature was 1223–1243 K for flux (1) and 1246 K for flux (2).

An optimal rate of temperature reduction for homogeneous crystallization is easier to control when crystal seeds are used. That is due to the fact that the number of crystals grown by spontaneous nucleation is unknown. Thus, the first step was to obtain seed crystals on a crystal carrier immersed in the flux by spontaneous nucleation. To achieve homogeneity, the flux was kept at T = 1000 °C for 24 h and then the temperature was reduced to $T = T_{sat} - 12°$ C. After 2 h, the crystal carrier was removed from the flux. As a result, a few crystallites formed on the crystal carrier from the cooled flux. The crystal carrier was then immersed again in the flux and rotated at 30 rpm with a change of direction every minute. In the next 24 h, 10–30 crystals 0.5–2 mm in size grew. They were of high quality and could be used as seeds.

For the next stage, a crystal carrier with four high-quality seeds less than 1 mm in size was suspended above the flux at T = 1000 °C. The temperature was then decreased to $T = T_{sat}$ + 7 °C. After that, the crystal holder with seeds was immersed in the flux to a depth of 25–30 mm and the rotation was started with a speed of 30 rpm and a reversal period of 1 min. Over 15 min, the temperature was reduced to $T = T_{sat} - 5$ °C. The temperature was then decreased by 1–3 °C per day according to a special program. In 9–13 d, the growth process was completed. The crystal carrier was lifted above the flux and cooled to room temperature in a furnace with the power off.

The grown crystals were about 6–10 mm in size, which is sufficient for studying their physical properties. Six single crystals from different series of the $Bi_2Mo_3O_{12}$ grown type (**samples 1–6**) and single crystals of the Li_2WO_4 grown type (**sample 7**) were selected for further analysis.

2.2. Elemental analysis

Qualitative elemental identification of all the crystals was performed by energy-dispersive X-ray fluorescence using an Orbis PC Micro-XRF Analyzer. This analysis was performed in a vacuum of 0.5 Torr with an accelerating voltage of 40 kV using two modes: with a 1 mm beam and an amplification time of 12.8 µs, and using a 30 µm beam with an amplification time of 1.6 µs. In addition, qualitative elemental analysis of **sample 2** and **sample 7** was performed by EDX elemental analysis using a FEI Osiris transmission electron microscope with a HAADF (high-angle annular dark-field) X-ray detector and an EDX analysis block Bruker SuperX at an accelerating voltage of 200 kV. For the latter measurements, single crystals were ground in a mortar and placed on a carbon-coated copper grid.

Both methods described above revealed a small amount of Bi atoms in the composition of **samples 1–6** grown using a $Bi_2Mo_3O_{12}$-based flux. There were no lines corresponding to Mo atoms for **samples 1–6** and no lines corresponding to W atoms for **sample 7** grown using Li_2WO_4 (Figs. S1 and S2 in the supporting information).

Quantitative elemental analysis of **sample 1** was performed using electron-probe X-ray spectral energy-dispersive microanalysis. The measurements were carried out on a polished surface under a carbon coating with a thickness of about 25 nm. A Jeol JSM-6480 LV scanning electron microscope with a tungsten thermionic cathode using an energy-dispersive spectrometer X-Max-N 50 (Oxford Instruments Ltd, UK) at an accelerating voltage of 20 kV and an electron probe current of 0.7 nA was used. The composition of the samples, averaged over seven atomic %ratio measurements, was Sm 5.07 (5):Bi 0.22 (2):Fe 15.80 (15):B 15.63 (46):O 63.29 (30). Therefore, the mutual Sm:Bi ratio for **sample 1**, based on energy-dispersive microanalysis data, is 0.96 (1):0.04 (1).

2.3. Single-crystal X-ray structure analysis

For the single-crystal X-ray structure analysis, the samples were prepared by chipping off the single crystals and giving them a spherical shape in an abrasive chamber using an air flow. **Samples 1–6** were made from each of six Bi-containing single crystals, and **samples 7(1)** and **7(2)** were prepared from Bi-free single crystals. The diameters of the samples selected were 0.17–0.32 mm.

X-ray diffraction (XRD) data were obtained for **samples 1–7** at room temperature, and for **sample 2** at set temperatures of 90, 200, 293 and 400 K. A CCD Xcalibur EOS S2 X-ray diffractometer (Rigaku Oxford Diffraction) with a Cobra Plus temperature attachment (Oxford Cryosystems) was used. Taking into account the previously obtained calibration curve (Dudka *et al.*, 2016), the temperature of the sample might be close to 98, 201, 293 and 397 K, respectively.

The temperature dependence of the unit-cell parameters a, b and c, and volume V of **sample 2** was measured in the temperature range 20–75 K with a step of 5 K using a single-crystal Huber-5042 diffractometer with a point detector, equipped with a closed-cycle helium cryostat DISPLEX DE-202 (Dudka *et al.*, 2017*a*,*b*). The temperature dependence of the unit-cell parameters of **sample 7(2)** was obtained in the range 11–94 K with a step of 5–10 K at the SNBL station of the ESRF, beamline BM01, using a PILATUS@SNBL diffractometer (Dyadkin *et al.*, 2016) with an ESRF Helijet flow cryostat (laminar helium gas stream cooling).

The temperature dependences of the unit-cell parameters obtained using Huber-5042 and PILATUS@SNBL diffractometers, as well as those calculated for the complete sets of Xcalibur EOS S2 diffraction data, are shown in Fig. 1. The temperature dependences of a, b, c and V obtained using the CCD Xcalibur diffractometer (which are shown in Fig. 1) were normalized to the curves obtained using the reference diffractometer Huber-5042, as described in Smirnova *et al.* (2022). PILATUS@SNBL experimental values were systematically lower than those of the Huber data, and they were shifted by parallel translation.

Table 1
Experimental details.

For all structures: $(Sm_{0.93}Bi_{0.07})Fe_3(BO_3)_4$, M_r = 557.2, trigonal, $R32$, Z = 3. Experiments were carried out with Mo $K\alpha$ radiation using a Rigaku Xcalibur EosS2 diffractometer with high θ cut. Absorption correction was for a sphere (*Jana2006*; Petříček *et al.*, 2014). Total number of refinement parameters was 36.

	90 K	**200 K**	**293 K**	**400 K**
Crystal data				
Temperature (K)	90	200	293	400
a, c (Å)	9.5638 (1), 7.5790 (1)	9.5635 (1), 7.5823 (1)	9.5642 (1), 7.5883 (1)	9.5650 (1), 7.5972 (1)
V (Å^3)	600.35 (1)	600.57 (1)	601.14 (1)	601.94 (1)
μ (mm^{-1})	13.66	13.66	13.65	13.63
Crystal radius (mm)	0.11 (1)	0.11 (1)	0.11 (1)	0.11 (1)
Data collection				
T_{min}, T_{max}	0.159, 0.254	0.159, 0.254	0.160, 0.255	0.116, 0.215
No. of measured, independent and observed [$I > 3\sigma(I)$] reflections	20719, 2769, 2769	20756, 2770, 2770	20806, 2774, 2772	20801, 2781, 2761
R_{int}	0.034	0.031	0.025	0.029
$(\sin\theta/\lambda)_{max}$ (Å^{-1})	1.354	1.355	1.355	1.355
Refinement				
$R[F^2 > 2\sigma(F^2)]$, $wR(F^2)$, S	0.011, 0.030, 1.08	0.011, 0.030, 1.04	0.012, 0.032, 1.04	0.012, 0.029, 1.03
No. of reflections	2769	2770	2774	2781
$\Delta\rho_{max}$, $\Delta\rho_{min}$ (e Å^{-3})	1.08, −0.95	0.96, −0.58	1.02, −0.63	0.83, −0.92
No. of Friedel pairs used in the refinement	1253	1253	1254	1259
Absolute structure parameter	0.028 (4)	0.030 (4)	0.031 (4)	0.028 (4)

Computer programs: *CrysAlis PRO* (Agilent, 2014; Rigaku OD, 2018) and *Jana2006* (Petříček *et al.*, 2014).

Table 2
Characteristic temperatures and static atomic displacements for $(Sm_{0.93}Bi_{0.07})Fe_3(BO_3)_4$.

Debye T_D and Einstein T_E characteristic temperatures, their difference ΔT_{DE}, values of zero-point oscillations $\langle u^2\rangle_{zero}$ and $\langle u^2\rangle_{shift}$ ($\langle u^2\rangle_{static} = \langle u^2\rangle_{zero} + \langle u^2\rangle_{shift}$) for cations in the $(Sm_{0.93}Bi_{0.07})Fe_3(BO_3)_4$ structure, and R factors of the model refinement. The top line for $\langle u^2\rangle_{zero}$ and $\langle u^2\rangle_{shift}$ is the Einstein approximation and the bottom line is the Debye approximation.

	T_E (K)	T_D (K)	ΔT_{DE}	$\langle u^2\rangle_{zero}$ (Å^2)	$\langle u^2\rangle_{shift}$ (Å^2)	R (%)
(Sm,Bi)	117 (2)	202 (3)	85	0.0013824	0.0005 (2)	1.45
				0.0011968	0.0005 (2)	1.45
Fe1	239 (6)	420 (10)	181	0.0018170	0.0004 (2)	1.98
				0.0015675	0.0005 (2)	2.15
O1	388 (5)	682 (12)	249	0.0039098	0.0001 (2)	1.02
				0.0033305	0.0001 (2)	1.53
O2	303 (4)	529 (5)	226	0.0050084	0.0004 (2)	1.03
				0.0043017	0.0005 (2)	0.78
O3	350 (3)	615 (7)	265	0.0043260	0.0001 (2)	0.76
				0.0036997	0.0003 (2)	0.86
B1	572 (8)	980 (8)	408	–	–	3.65
						2.19
B2	521 (8)	895 (6)	374	–	–	3.32
						1.64

The diffraction peaks were integrated using the *CrysAlis PRO* software (Rigaku OD, 2018). The structures were refined using the *Jana2006* program (Petříček *et al.*, 2014) by the least-squares method. The absolute configuration was considered by refining the ratio of the volumes of the racemic twin components (Flack & Bernardinelli, 1999; *Online Dictionary of Crystallography*, 2019*b*). Taking into account the extinction effect, the best Becker–Coppens model (Becker & Coppens, 1974) was selected for each of the experiments, where the orientation of the mosaic blocks is distributed according to the Lorentz law (type 1).

The details and refinement results of the experiments carried out at different temperatures for **sample 2** are given in Table 1. Atomic coordinates, equivalent displacement parameters and the main interatomic distances for **sample 2** at different temperatures, as well as the experimental conditions and a comparison of the structure refinement for **samples 1–7** at room temperature, are given in the supporting information.

The unit-cell parameters calculated by *CrysAlis PRO* (not normalized) presented in Table 1 were used to refine and correctly compare the interatomic distances in samarium iron borate with the data previously obtained using a CCD Xcalibur diffractometer for the other rare-earth iron borate single crystals (Smirnova *et al.*, 2018, 2019, 2022).

Based on the values of the equivalent isotropic atomic displacement parameters U_{eq} obtained for each of the atoms in four temperature experiments, the characteristic Debye temperature (T_D) and Einstein temperature (T_E) were calculated (Table 2) using extended models by the method of Dudka *et al.* (2019). The static disordering $\langle u^2\rangle_{shift}$ has not been refined for the light B atoms.

2.4. Mössbauer spectroscopy

To carry out Mössbauer experiments, powder samples of bismuth-containing samarium iron borate with a mass of 20 (1) mg were prepared from single crystals. For this purpose, small portions of the single crystals were pre-ground in an agate mortar, then the resulting powder was poured into a thin-walled cylindrical container 8 mm in diameter made of thin aluminium foil and pressed lightly. Mössbauer absorption spectra for ^{57}Fe nuclei were obtained in the temperature range 9–295 K in the constant acceleration regime using a standard

MS-1104Em spectrometer equipped with a closed-cycle helium cryostat RTI CryoFree-104 (Naumov *et al.*, 2010). The ^{57}Co (Rh) γ-ray source Ritverc MCo7.114 (https://ritverc.com/) was at room temperature. The isomer shifts were measured relative to a reference absorber Ritverc MRA.2.6 (30 µm thickness α-Fe foil at room temperature). Computer analysis of the Mössbauer spectra was performed using the program *Univem MS*, the software supplied with the spectrometer MS-1104Em.

3. Bi content and absolute structure configuration

The structure of the $(Sm_{0.93}Bi_{0.07})Fe_3(BO_3)_4$ single crystal at T = 90, 200, 293 and 400 K was refined in the space group $R32$ (Z = 3). Analysis of the systematic absences (Hahn, 2006) did not reveal structural phase transitions in the temperature range 90–400 K.

The Sm:Bi ratio for all the samples was obtained from XRD data by refining the occupancy of the Sm and Bi atoms in the 3*a* Wyckoff position [identical coordinates and anisotropic displacement parameters (ADPs) were used, and the overall sum was restrained]. Refinement of the Sm occupancy factor in the 3*a* position without including Bi in the structure revealed an increase in the Sm occupancy. Whereas the Fe occupancy factor, refined in the 9*d* positions, did not demonstrate any noticeable deviation. That proves the partial substitution of Sm atoms by Bi atoms and the absence of impurity atoms in the Fe 9*d* position. Refining of the Sm occupancy factor for the samples without Bi revealed a slight decrease in its value.

The Sm:Bi ratio for samples from different series is uniform and its averaged value according to XRD data is 0.93 (2): 0.07 (2). These results are consistent with the data for a low degree of Bi incorporation obtained from X-ray spectral energy-dispersive microanalysis.

Based on four sets of temperature dependence data obtained from the diffraction analysis for **sample 2**, the average Sm:Bi ratio is 0.932 (6):0.068 (6). Therefore, the formula $(Sm_{0.93}Bi_{0.07})Fe_3(BO_3)_4$ was used for the final refinement.

Refinement of the Flack parameter revealed different absolute configurations of **samples 1–7. Samples 1–3** and **7(2)** turned out to be almost monodomain, whereas **samples 4–6** and **7(1)** were racemic twins, with both enantiomorph components (Fig. 2) present in the structure in a close ratio of 0.4 (1):0.6 (1) for different samples.

Thus, rare-earth iron borate crystals grown by the same technique both with $Bi_2Mo_3O_{12}$- and Li_2WO_4-based fluxes (Gudim *et al.*, 2010; Eremin *et al.*, 2019) can be multi- or monodomain. This should be taken into account when studying optical and magnetoelectric properties, which are affected by chirality.

4. Temperature dependence of the unit-cell parameters

The general character of the temperature dependence of the unit-cell parameters of samarium iron borate is similar to that of neodymium iron borate (Smirnova *et al.*, 2022) without the $R32 \rightarrow P3_121$ ($P3_221$) structural phase transition.

The unit-cell parameter a of samarium iron borate decreases smoothly by $\simeq$0.0012 Å with decreasing temperature from 400 to 90 K, and it varies by no more than 0.0004 Å at temperatures between 90 and 11 K. The unit-cell changes in the c direction are more pronounced than in the ab plane. The c parameter decreases noticeably by $\simeq$0.02 Å at temperatures between 400 and 90 K and demonstrates an anomalous growth by $\simeq$0.002 Å in the range 80–30 K. Parameter c continues to grow with the temperature decreasing to 20 K based on Huber-5042 data, but there is a slight decrease of c below 30 K based on PILATUS@SNBL data (Fig. 1).

It is noteworthy that the same character of the c anomalous temperature dependence in the range 80–30 K is observed for Bi-containing **sample 2**, measured using a laboratory diffractometer, and for **sample 7(2)** without Bi, measured using synchrotron radiation. Moreover, these samples are monodomain, whereas such an effect was observed also for the rare-earth iron borates having two microdomain components of close ratio (Smirnova *et al.*, 2018).

This observation is further evidence that the anomalous increase of c below 80 K is a characteristic feature of the rare-earth iron borate family, regardless of the rare-earth ion, bismuth content, twin components present and the existence of the $R32 \rightarrow P3_121$ structural phase transition (Smirnova *et al.*, 2019, 2022).

Following the a and c changes, the unit-cell volume decreases by $\simeq$0.6 Å^3 with decreasing temperature from 400 to 90 K and then increases slightly by $\simeq$0.1 Å^3 at temperatures down to 11 K.

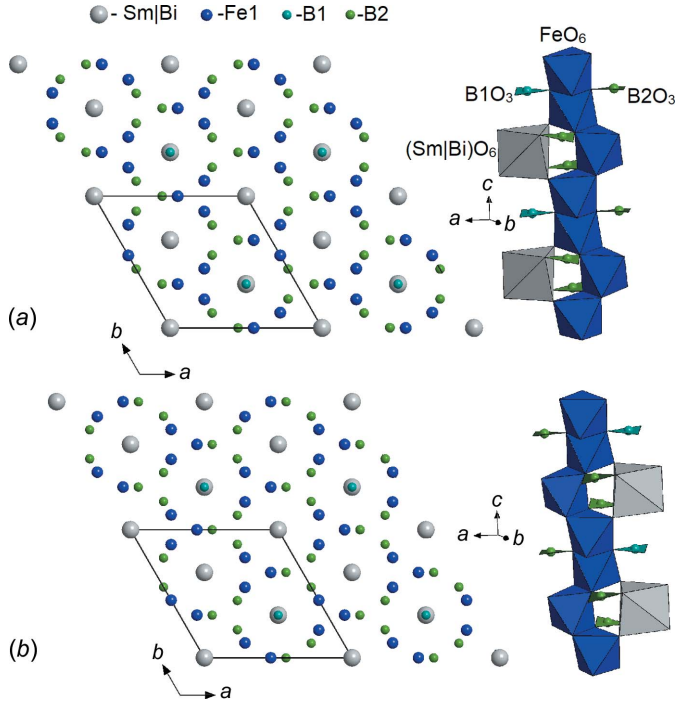

Figure 2
A unit cell for the (*a*) right-handed and (*b*) left-handed microdomain configurations of $(Sm_{0.93}Bi_{0.07})Fe_3(BO_3)_4$ in the space group $R32$.

The *a* and *c* unit-cell parameters of $(Sm_{0.93}Bi_{0.07})Fe_3(BO_3)_4$ (not normalized; Table 1) are lower than those of $(Nd_{0.91}Bi_{0.09})Fe_3(BO_3)_4$ but larger than those of both $(Y_{0.95}Bi_{0.05})Fe_3(BO_3)_4$ (Smirnova *et al.*, 2018) and $(Ho_{0.96}Bi_{0.04})Fe_3(BO_3)_4$ (Smirnova *et al.*, 2019) measured using the same diffractometer at the same temperatures, consistent with the ionic radii of the rare-earth elements.

The averaged unit-cell parameters at room temperature for the bismuth-containing **samples 1–6** are a = 9.5665 (5) and c = 7.5901 (9) Å, and for **samples 7(1)** and **7(2)** without Bi are a = 9.5670 (8) and c = 7.5908 (4) Å (not normalized). It could be concluded that, within the existing instrumental error, single-crystal X-ray diffraction does not allow one to distinguish unambiguously structural features between the samples with and without Bi due to its low concentration. In particular, this is true for the comparison of the interatomic bonds and atomic displacement parameters. Therefore, the following temperature analysis is described only for the Bi-containing monodomain **sample 2**.

5. Interatomic distances and bond angles

A general view of the samarium iron borate structure is shown in Fig. 3.

A slight decrease in the lengths of the (Sm,Bi)—O exchange bonds in the $(Sm,Bi)O_6$ distorted trigonal prisms is observed with decreasing temperature [Fig. 4(*a*)], as well as a decrease of the Sm—B and Sm—Fe distances to the next coordination sphere. Over the entire temperature range, the Sm—O bond lengths are longer than the *R*—O distances in the Y and Ho compounds, but shorter than the Nd—O bond lengths in the neodymium compound [Fig. 4(*a*)], which is in agreement with the ionic radii of the rare-earth elements. The Sm—B and Sm—Fe distances [Fig. 4(*b*)] are shorter than the Nd—B and Nd—Fe distances in neodymium iron borate. The Sm—Fe distance in the high-temperature region exceeds the corresponding distance in the rare-earth iron borates with *R* = Y and Ho. Below T_{str} for borates with *R* = Y and Ho (where a distortion of the Fe—Fe distances in different iron chains appear), the Sm—Fe distance is comparable to the *R*—Fe1 distance to the Fe atoms from the Fe1-type chain [Fig. 4(*b*)].

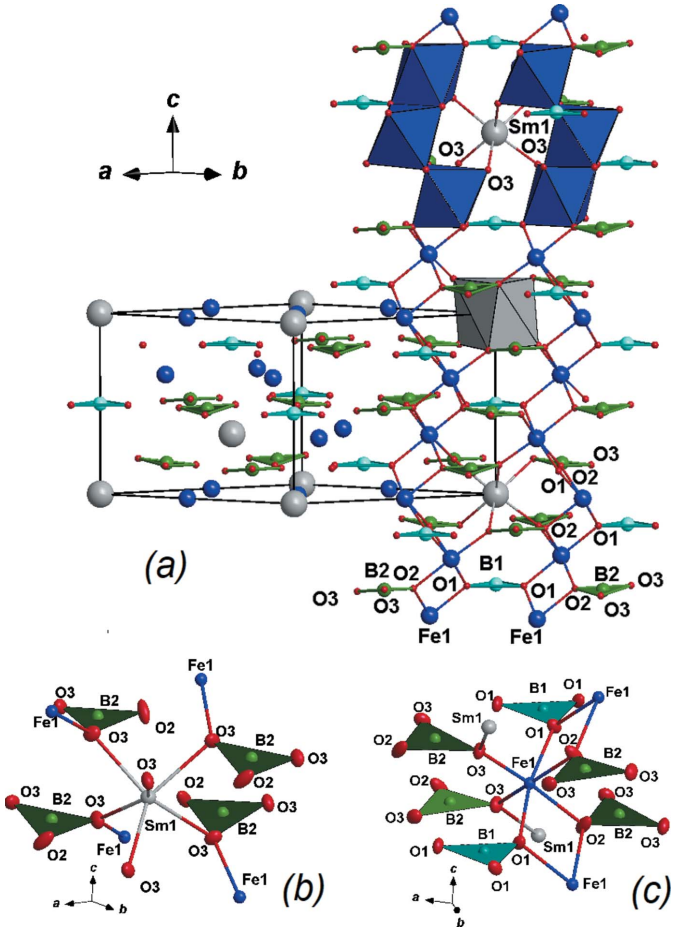

Figure 3
(*a*) A general view of the $(Sm_{0.93}Bi_{0.07})Fe_3(BO_3)_4$ structure at 400 K. The arrangement of the coordination polyhedra and the Fe chains is shown. (*b*) The local environments of the Sm(Bi) atoms in the structure. (*c*) The local environments of the Fe atoms in the structure. In the lower parts, the atoms are shown as displacement ellipsoids at the 80% probability level.

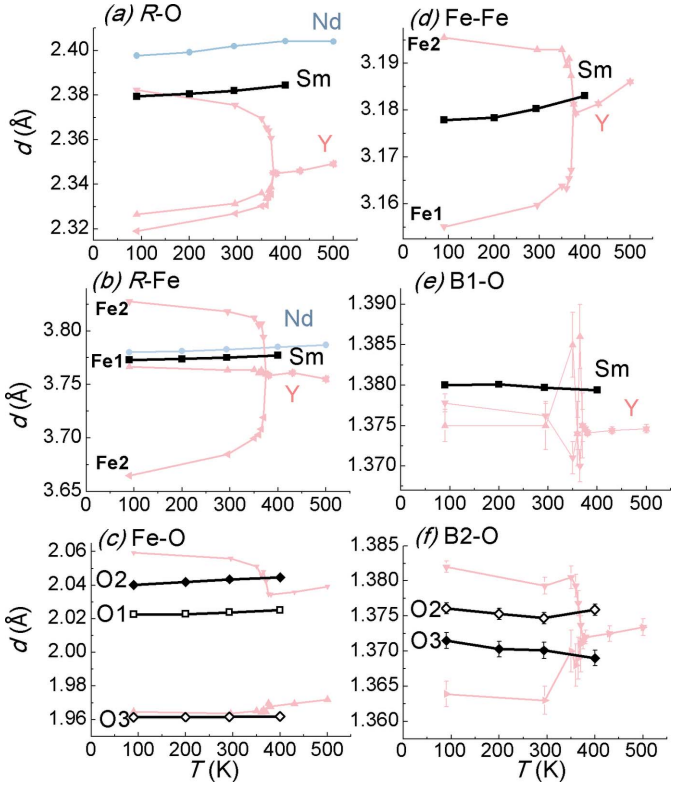

Figure 4
The temperature dependences of the interatomic distances in the structure of $(Sm_{0.93}Bi_{0.07})Fe_3(BO_3)_4$ demonstrated in comparison with those for the structures of $(Y_{0.95}Bi_{0.05})Fe_3(BO_3)_4$ (Smirnova *et al.*, 2018) and $(Nd_{0.91}Bi_{0.09})Fe_3(BO_3)_4$ (Smirnova *et al.*, 2022). The distances in $(Sm_{0.93}Bi_{0.07})Fe_3(BO_3)_4$ are shown in black and the corresponding distances in the structures with *R* = Nd and Y are shown in light-blue and light-pink, respectively. They are the following: (*a*) Sm—O in the SmO_6 prism; (*b*) Sm—Fe to the nearest Fe atoms; (*c*) Fe—O in the FeO_6 octahedron (for *R* = Y, the maximal and minimal Fe—O distances are shown); (*d*) Fe—Fe in the iron chains (Fe1—Fe1 and Fe2—Fe2 in the case of *R* = Y); (*e*) B1—O in the $B1O_3$ triangle; (*f*) B2—O in the $B2O_3$ triangle (for *R* = Y, the maximal and minimal B—O distances are shown).

The average Fe—O distance in the FeO_6 octahedra [Fig. 4(*c*)] and their distortion are comparable to those for neodymium iron borate. The average Fe—O distance decreases with temperature by ≃0.003 Å, and the difference between the maximal and minimal Fe—O distances in the FeO_6 octahedron decreases by ≃0.005 Å.

The Fe—Fe distances between Fe atoms in the Fe–Fe chains [Fig. 4(*d*)] and between the chains themselves decrease uniformly with temperature. The Fe—Fe distances in the Sm compound are slightly shorter than in the Nd compound. The Fe—B distances to the nearest B1 and B2 atoms decrease or do not change.

The Fe—Fe chains bend slightly with decreasing temperature. The Fe—O1—Fe angles in a separate iron chain decrease slightly with decreasing temperature from 103.61 (1)° at 400 K to 103.56 (1)° at 90 K, while the Fe—O2—Fe angles increase slightly from 102.23 (1)° at 400 K to 102.31 (1)° at 90 K.

The B1—O distances in the $B1O_3$ triangle [Fig. 4(*e*)] changes by less than 0.001 Å in the temperature range 90–400 K. The average B2—O distance in the $B2O_3$ triangle [Fig. 4(*f*)] increases slightly by ≃0.002 Å with decreasing temperature.

While the $B1O_3$ triangles are oriented parallel to the *ab* plane, the $B2O_3$ triangles deviate from it with decreasing temperature. This deviation has the same character as for the neodymium compound, but is slightly lower for samarium iron borate.

From the above analysis, it can be stated that the characteristic distances in the $(Sm_{0.93}Bi_{0.07})Fe_3(BO_3)_4$ structure change in a similar manner to those in the Nd compound. These changes are also similar to those for the compounds with R = Ho and Y, which occur before the phase transition from the space group $R32$ to the space group $P3_121$ (above $T_{str} \simeq 365$–370 K). At high temperatures, the main differences in the bond lengths for the four of these compounds is seen for the R—O distance, which results from the different ionic radii of the rare-earth elements.

6. Atomic displacement parameters and characteristic temperatures

The equivalent isotropic displacement parameters U_{eq} of all the atoms in the $(Sm_{0.93}Bi_{0.07})Fe_3(BO_3)_4$ structure decrease uniformly with decreasing temperature from 400 to 90 K (Fig. 5). The temperature dependence of $U_{eq}(T)$ (Fig. 5) is fitted by model curves in the extended Debye approximation (Dudka *et al.*, 2019). The model curves in the extended Einstein approximation have a similar character. The temperature dependences of $U_{eq}(T)$ are well described by a one-component model in the Debye or Einstein approximation, which additionally proves the absence of a structural phase transition in the temperature range 90–400 K.

Similar to the iron borates with R = Nd, Ho and Y, the U_{eq} parameters of the R (Sm) and O2 atoms change most rapidly with temperature, and the flattest $U_{eq}(T)$ dependence is for the B1 atoms. Such an advanced decrease in the vibrations of the Sm and O2 atoms can affect the magnetoelectric properties below the Néel temperature.

The highest U_{eq} values and the most elongated atomic displacement ellipsoids are for the O2 atoms, which connect the $B2O_3$ triangles with the iron chains [Figs. 3(*b*) and 3(*c*)].

The Debye (T_D) and Einstein (T_E) temperatures calculated for all the atoms in the structure using model curves based on experimental U_{eq} values and their difference ($\Delta T_{DE} = T_D - T_E$) are given in Table 2.

The highest values of T_D and T_E, which indicate the strongest interaction with neighbouring atoms, correspond to B atoms, similar to that for the previously studied rare-earth iron borates with R = Nd, Ho and Y. B atoms have the largest ΔT_{DE}, that is the largest difference between the average and maximum vibration frequencies. This implies the largest possible number of vibrational modes.

The lowest T_D and T_E and the smallest ΔT_{DE} is observed for the Sm atoms, resulting in the weakest interaction of Sm with neighbouring atoms, together with the lowest possible number of vibrational modes.

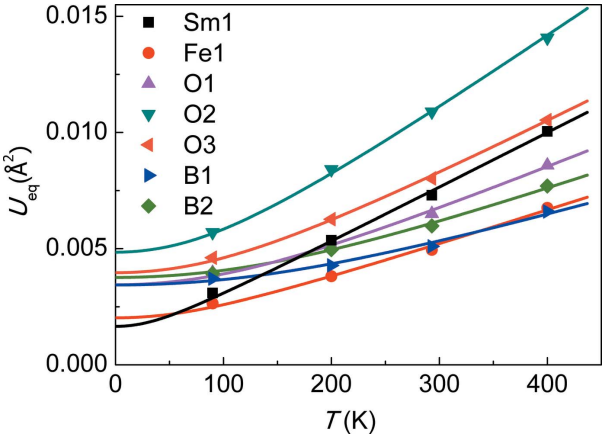

Figure 5
The temperature dependence of the equivalent isotropic atomic displacement parameters for all the atoms in $(Sm_{0.93}Bi_{0.07})Fe_3(BO_3)_4$. The symbols show the experimental values and the solid lines are the model curves plotted in the Debye extended approximations.

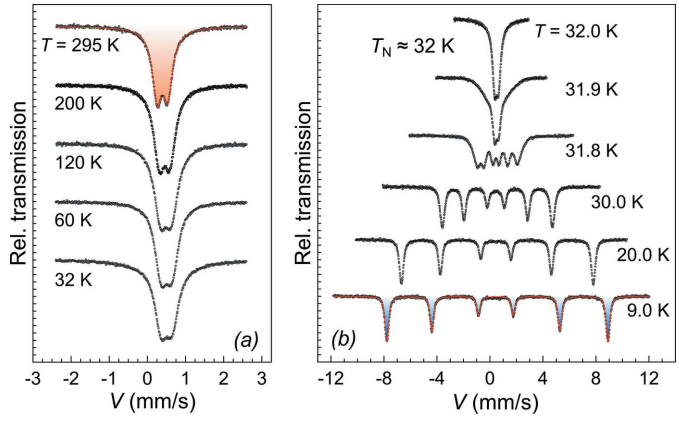

Figure 6
Mössbauer spectra of the $SmFe_3(BO_3)_4$ powder sample at several temperatures (*a*) above and (*b*) below the magnetic phase transition point $T_N \simeq 32$ K.

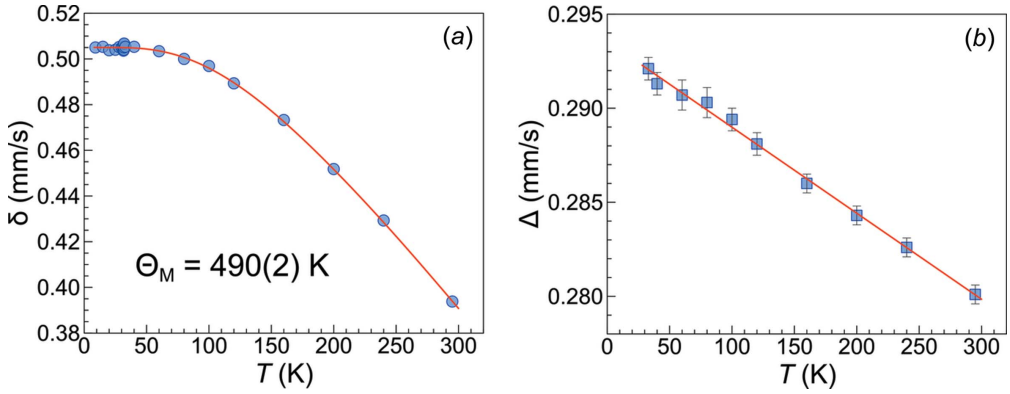

Figure 7
(*a*) The temperature dependence of the isomer shift $\delta(T)$; the solid red line is the calculated curve obtained in an approximation of the second-order Doppler effect. (*b*) The temperature dependence of the quadrupole splitting $\Delta(T)$; the solid red line was obtained in the least-squares linear approximation.

As for O atoms, the lowest T_D and T_E values and the lowest ΔT_{DE} value are observed for O2 atoms. This indicates that the O2 atoms, in addition to the most pronounced atomic displacements U_{eq} and the most elongated atomic displacement ellipsoids, have the lowest possible number of vibrational modes of all the O atoms. The described effect agrees with the results for the Sm and Fe atoms. The atomic displacement parameters U_{eq} for Sm are higher than those for Fe, and the number of vibrational modes (difference ΔT_{DE}) is lower for the Sm atoms.

7. Mössbauer hyperfine parameters

The Mössbauer spectra of the bismuth-containing $SmFe_3(BO_3)_4$ powder sample at different temperatures are shown in Fig. 6. At temperatures above $T \simeq 32$ K, the spectra are described by a simple doublet typical of the paramagnetic state of the iron ions. The spectra are similar with respect to shape and parameters to those observed in bismuth-containing $GdFe_3(BO_3)_4$ (Frolov *et al.*, 2016) and $YFe_3(BO_3)_4$ crystals (Frolov *et al.*, 2018); the line intensities in the doublet are slightly asymmetric due to the texture effect [Fig. 6(*a*)]. All the paramagnetic spectra of $SmFe_3(BO_3)_4$ are well approximated by a single doublet with isomer shift δ and quadrupole splitting Δ values corresponding to the high-spin state ($S = 5/2$) of Fe^{3+} ions in an octahedral oxygen environment [Fig. 6(*a*)].

Fig. 7 shows the temperature dependences of the hyperfine parameters $\delta(T)$ and $\Delta(T)$ in the paramagnetic temperature range. The 'Mössbauer' Debye temperature Θ_M = 490 (2) K, which characterizes the stiffness of the bonds of the Fe atoms in the $SmFe_3(BO_3)_4$ crystal structure, was calculated from the dependence of the isomer shift on temperature $\delta(T)$ using a standard procedure (Gütlich *et al.*, 2011; Herber, 1984). The value of Θ_M agrees with the Debye vibration temperature T_D = 420 (10) K of Fe ions, obtained from the data of single-crystal X-ray diffraction measurements. The value of the quadrupole splitting Δ increases linearly from 0.280 to 0.292 mm s^{-1} with decreasing temperature from 295 to 32 K [Fig. 7(*b*)]. As was shown for the rare-earth iron borates with R = Y, Ho, Gd and Nd (Frolov *et al.*, 2016, 2018; Smirnova *et al.*, 2019, 2022), the quadrupole splitting in these compounds is sensitive to structural changes. For these crystals, the local maximum appears in the $\Delta(T)$ dependence in the region of the structural phase transition, and $\Delta(T)$ demonstrates an inflection below 100–160 K, which is close to the region of negative thermal expansion of the unit-cell parameter *c*. The inflections of the $\Delta(T)$ curve in the region of negative thermal expansion is observed also for the crystal with Nd, where there is no structural phase transition, but the magnetic phase transition exists. However, for the samarium compound, this dependence is close to linear. Such a difference in $\Delta(T)$ dependence for different rare-earth iron borates is of interest and requires additional analysis.

Below T = 32 K, the Mössbauer spectra show a characteristic magnetic splitting [Fig. 6(*b*)], which indicates the magnetic ordering of the iron ions. All the spectra are well approximated by a single magnetic sextet. This indicates that all the iron ions are in magnetically equivalent structural sites.

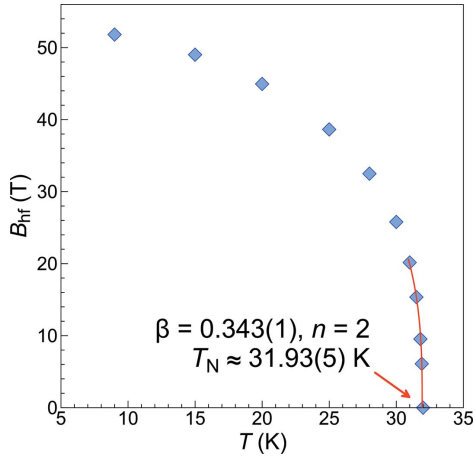

Figure 8
The temperature dependence of the magnetic hyperfine field B_{hf} at the iron nuclei in $SmFe_3(BO_3)_4$. The solid red line is the calculated curve obtained in an approximation of the critical coefficient model.

The calculated parameters of the magnetic hyperfine interactions for different temperatures below the magnetic phase transition are given in the supporting information.

Fig. 8 shows the temperature dependence of the average value of the magnetic hyperfine field B_{hf} at ^{57}Fe nuclei for iron ions in $SmFe_3(BO_3)_4$. Refinement of the magnetic phase transition temperature T_N and determination of the type and dimension of the iron subsystem magnetic ordering were carried out the same way as in Frolov *et al.* (2016, 2018). The experimental dependence of $B_{hf}(T)$ near T_N was approximated using the model of critical coefficients $B(T) = B_0(1 - T/T_N)^{\beta}$ (Stanley, 1971). A more detailed description is given in the supporting information.

As a result of the calculations for the $SmFe_3(BO_3)_4$ crystal, the values T_N = 31.93 (5) K and β = 0.343 (1) (n = 2) were obtained, which are characteristic of the three-dimensional planar XY model. These results are in good agreement with the results of spectroscopic (Chukalina *et al.*, 2010) and neutron diffraction (Ritter *et al.*, 2012) studies of the magnetic structure below T_N, which revealed the non-Brillouin increase in the magnetic moment of iron, and the formation of strong interactions between the iron and samarium substructures, leading to the appearance of the long-range easy-plane type magnetic order.

8. Summary

The single-crystal structure and Mössbauer hyperfine parameters of samarium iron borate have been studied.

Bi atoms entered the composition of single crystals grown using the $Bi_2Mo_3O_{12}$-based flux and no impurities were revealed in the single crystal grown using the Li_2WO_4-based flux. The average Sm:Bi ratio in the Bi-containing samples based on XRD analysis was 0.93 (2):0.07 (2).

Different absolute configurations of the samples grown using both fluxes were demonstrated; the samples were monodomain or racemic twins with both enantiomorph components present in a close ratio of 0.4 (1):0.6 (1). Thus, the rare-earth iron borate crystals grown under the same conditions using both fluxes can be multi- or monodomain, which should be taken into account when studying optical and magnetoelectric properties affected by chirality.

The a unit-cell parameter of samarium iron borate decreases smoothly from 400 K to 90 K, and barely changes between 90 K and 11 K. The c unit-cell parameter decreases noticeably from 400 K to 90 K and demonstrates an anomalous increase below 80 K. The presence of negative thermal expansion in the c direction observed in rare-earth iron borates seems to be independent of the presence of bismuth atoms, of the racemic twin component ratio and of the existence of the $R32 \rightarrow P3_121$ structural phase transition in the low-temperature region.

The smooth change of the unit-cell parameters over the temperature range 11–400 K, as well as the monotonic temperature dependence of the interatomic distances and equivalent isotropic atomic displacement parameters in the range 90–400 K confirm the absence of a structural phase transition.

No significant difference in the structural parameters of the samples grown using $Bi_2Mo_3O_{12}$- and Li_2WO_4-based fluxes was observed.

It was confirmed that the structure of $(Sm_{0.93}Bi_{0.07})Fe_3(BO_3)_4$ belongs to the space group $R32$ at 90–400 K. With a lowering of the temperature in this range, a decrease in the (Sm,Bi)—O, Sm—B, Sm—Fe, Fe—O, Fe—B1, Fe—B2 and Fe—Fe distances (in chains and between them) was observed, B1—O did not change and the average B2—O distance increased slightly. The Fe–Fe chains bend slightly with decreasing temperature.

The equivalent isotropic atomic displacement parameters U_{eq} of all the atoms in the $(Sm_{0.93}Bi_{0.07})Fe_3(BO_3)_4$ structure decrease uniformly with decreasing temperature from 400 K to 90 K. The strongest decrease of U_{eq} is for Sm and O2 and the weakest one is for B1. The O2 atoms have the highest U_{eq} values, the most elongated atomic displacement ellipsoids of all the atoms and the smallest number of possible vibrational modes of all O atoms. The highest values of the Debye and Einstein temperatures (T_D and T_E, respectively) and the highest ΔT_{DE} are for B atoms, which corresponds to their largest number of allowed vibrational modes and their strongest interaction with their surroundings. The lowest T_D and T_E and the smallest ΔT_{DE} are for the Sm atoms.

Mössbauer measurements on bismuth-containing $SmFe_3(BO_3)_4$ confirmed that the Fe^{3+} ions are in a high-spin state (S = 5/2) in the octahedral oxygen environment. The 'Mössbauer' Debye temperature Θ_M = 490 (2) K calculated from the isomer shift temperature dependence $\delta(T)$ is consistent with the Debye temperature T_D = 420 (10) K of the Fe ions, obtained using the data from the single-crystal X-ray diffraction measurements.

The temperature dependence of the quadrupole splitting $\Delta(T)$ of the paramagnetic Mössbauer spectra shows a linear increase upon cooling and does not have any anomalies, in contrast to other iron borates studied earlier.

The Néel temperature T_N = 31.93 (5) K was found from the temperature dependence of the hyperfine magnetic field $B_{hf}(T)$. An analysis of $B_{hf}(T)$ revealed the non-Brillouin character of the dependence and confirmed the easy-plane type of the long-range magnetic order in $SmFe_3(BO_3)_4$ below T_N.

Acknowledgements

The authors are grateful to D. Yu. Chernyshov (SNBL, ESRF, Grenoble) for assistance in obtaining the experimental data. This work was performed using the equipment of the Shared Research Center FSRC 'Crystallography and Photonics' RAS supported by the Russian Ministry of Science and Higher Education. This work was supported by the Ministry of Science and Higher Education within the State assignment FSRC 'Crystallography and Photonics' RAS.

References

Agilent (2014). *CrysAlis PRO*. Version 1.171.39.46. Rigaku Oxford Diffraction Ltd, Yarnton, Oxfordshire, England.

Becker, P. J. & Coppens, P. (1974). *Acta Cryst.* A**30**, 129–147.

Boldyrev, K. N., Burlakov, V. M., Gudim, I. A., Gavrilkin, S. Yu. & Popova, M. N. (2021). *Phys. Rev. Mater.* **5**, 094414.

Boldyrev, K. N., Popova, M. N., Bettinelli, M., Temerov, V. L., Gudim, I. A., Bezmaternykh, L. N., Loiseau, P., Aka, G. & Leonyuk, N. I. (2012). *Opt. Mater.* **34**, 1885–1889.

Campá, J. A., Cascales, C., Gutiérrez-Puebla, E., Monge, M. A., Rasines, I. & Ruíz-Valero, C. (1997). *Chem. Mater.* **9**, 237–240.

Cheong, S. W. & Mostovoy, M. (2007). *Nat. Mater.* **6**, 13–20.

Chukalina, E. P., Popova, M. N., Bezmaternykh, L. N. & Gudim, I. A. (2010). *Phys. Lett. A*, **374**, 1790–1792.

Condon, E. U. (1937). *Rev. Mod. Phys.* **9**, 432–457.

Dudka, A. P., Antipin, A. M. & Verin, I. A. (2017*a*). *Crystallogr. Rep.* **62**, 797–801.

Dudka, A. P., Bolotina, N. B. & Khrykina, O. N. (2019). *J. Appl. Cryst.* **52**, 690–692.

Dudka, A. P., Smirnova, E. S., Verin, I. A. & Bolotina, N. B. (2017*b*). *Crystallogr. Rep.* **62**, 651–659.

Dudka, A. P., Verin, I. A. & Smirnova, E. S. (2016). *Crystallogr. Rep.* **61**, 692–696.

Dyadkin, V., Pattison, P., Dmitriev, V. & Chernyshov, D. (2016). *J. Synchrotron Rad.* **23**, 825–829.

Eremin, E., Gudim, I., Temerov, V., Smolyakov, D. & Molokeev, M. (2019). *J. Cryst. Growth*, **518**, 1–4.

Erofeev, D. A., Chukalina, E. P., Bezmaternykh, L. N., Gudim, I. A. & Popova, M. N. (2016). *Opt. Spectrosc.* **120**, 558–565.

Flack, H. D. & Bernardinelli, G. (1999). *Acta Cryst.* A**55**, 908–915.

Frolov, K. V., Lyubutin, I. S., Alekseeva, O. A., Smirnova, E. S., Verin, I. A., Temerov, V. L., Bezmaternykh, L. N., Gudim, I. A., Artemov, V. V. & Dmitrieva, T. V. (2018). *J. Alloys Compd.* **748**, 989–994.

Frolov, K. V., Lyubutin, I. S., Smirnova, E. S., Alekseeva, O. A., Verin, I. A., Artemov, V. V., Kharlamova, S. A., Bezmaternykh, L. N. & Gudim, I. A. (2016). *J. Alloys Compd.* **671**, 545–551.

Gudim, I. A., Eremin, E. V. & Temerov, V. L. (2010). *J. Cryst. Growth*, **312**, 2427–2430.

Gütlich, P., Bill, E. & Trautwein, A. X. (2011). *Mössbauer Spectroscopy and Transition Metal Chemistry: Fundamentals and Applications*, pp. 81–83. Berlin, Heidelberg: Springer.

Hahn, Th. (2006). *International Tables for Crystallography*, Vol. A, *Space-group symmetry*, 1st online ed., edited by Th. Hahn. Chester: International Union of Crystallography.

Herber, R. H. (1984). *Chemical Mossbauer Spectroscopy*, edited by R. H. Herber, pp. 199–205. New York: Plenum.

Hinatsu, Yu., Doi, Y., Ito, K., Wakeshima, M. & Alemi, A. (2003). *J. Solid State Chem.* **172**, 438–445.

Kadomtseva, A. M., Popov, Yu. F., Vorob'ev, G. P., Pyatakov, A. P., Krotov, S. S., Kamilov, K. I., Ivanov, V., Mukhin, A. A., Zvezdin, A. K., Kuz'menko, A. M., Bezmaternykh, L. N., Gudim, I. A. & Temerov, V. L. (2010). *Low Temp. Phys.* **36**, 511–521.

Klimin, S. A., Fausti, D., Meetsma, A., Bezmaternykh, L. N., van Loosdrecht, P. H. M. & Palstra, T. T. M. (2005). *Acta Cryst.* B**61**, 481–485.

Mukhin, A. A., Vorob'ev, G. P., Ivanov, V. Y., Kadomtseva, A. M., Narizhnaya, A. S., Kuz'menko, A. M., Popov, Y. F., Bezmaternykh, L. N. & Gudim, I. A. (2011). *JETP Lett.* **93**, 275–281.

Naumov, P. G., Lyubutin, I. S., Frolov, K. V. & Demikhov, E. I. (2010). *Instrum. Exp. Tech.* **53**, 770–776.

Online Dictionary of Crystallography (2017). *Chiral space groups*. https://dictionary.iucr.org/Chiral_space_group.

Online Dictionary of Crystallography (2019*a*). *Sohncke groups*. https://dictionary.iucr.org/Sohncke_groups.

Online Dictionary of Crystallography (2019*b*). *Flack parameter*. https://dictionary.iucr.org/Flack_parameter.

Petříček, V., Dušek, M. & Palatinus, L. (2014). *Z. Kristallogr.* **229**, 345–352.

Platunov, M. S., Gudim, I. A., Ovchinnikova, E. N., Kozlovskaya, K. A., Wilhelm, F., Rogalev, A., Hen, A., Ivanov, V. Y., Mukhin, A. A. & Dmitrienko, V. E. (2021). *Crystals*, **11**, 531.

Popova, M. N., Chukalina, E. P., Boldyrev, K. N., Stanislavchuk, T. N., Malkin, B. Z. & Gudim, I. A. (2017). *Phys. Rev. B*, **95**, 125131.

Popova, M. N., Malkin, B. Z., Boldyrev, K. N., Stanislavchuk, T. N., Erofeev, D. A., Temerov, V. L. & Gudim, I. A. (2016). *Phys. Rev. B*, **94**, 184418.

Popov, Yu. F., Pyatakov, A. P., Kadomtseva, A. M., Vorob'ev, G. P., Zvezdin, A. K., Mukhin, A. A., Ivanov, V. Yu. & Gudim, I. A. (2010). *J. Exp. Theor. Phys.* **111**, 199–203.

Rigaku OD (2018). *CrysAlis PRO*. Version 1.171.39.46. Rigaku Oxford Diffraction Ltd, Yarnton, Oxfordshire, England.

Ritter, C., Pankrats, A., Gudim, I. & Vorotynov, A. (2012). *J. Phys. Condens. Matter*, **24**, 386002.

Smirnova, E. S., Alekseeva, O. A., Dudka, A. P., Artemov, V. V., Zubavichus, Y. V., Gudim, I. A., Bezmaterhykh, L. N., Frolov, K. V. & Lyubutin, I. S. (2018). *Acta Cryst.* B**74**, 226–238.

Smirnova, E. S., Alekseeva, O. A., Dudka, A. P., Khmelenin, D. N., Frolov, K. V., Lyubutina, M. V., Gudim, I. A. & Lyubutin, I. S. (2019). *Acta Cryst.* B**75**, 954–968.

Smirnova, E. S., Alekseeva, O. A., Dudka, A. P., Verin, I. A., Artemov, V. V., Bezmaternykh, L. N., Gudim, I. A., Frolov, K. V. & Lyubutin, I. S. (2016). *Crystallogr. Rep.* **61**, 558–565.

Smirnova, E. S., Alekseeva, O. A., Dudka, A. P., Verin, I. A., Artemov, V. V., Lyubutina, M. V., Gudim, I. A., Frolov, K. V. & Lyubutin, I. S. (2022). *Acta Cryst.* B**78**, 1–13.

Stanley, H. E. (1971). *Introduction to Phase Transitions and Critical Phenomena*, edited by H. E. Stanley, pp. 42–49. Oxford: Clarendon Press.

Usui, T., Tanaka, Y., Nakajima, H., Taguchi, M., Chainani, A., Oura, M., Shin, S., Katayama, N., Sawa, H., Wakabayashi, Y. & Kimura, Y. (2014). *Nat. Mater.* **13**, 611–618.